Small

NANO · MICRO small
www.small-journal.com

RESEARCH ARTICLE OPEN ACCESS

Physical Anchoring-Assisted Mechanically Guided Assembly for Material-Independent 3D Mesostructures

Yeonhee Heo[1] | Pei Liu[2] | Jeongmin Yoo[1] | Jae Hyuk Hwang[3] | Gooyoon Chung[1] | Dong-Gyun Kim[3,4] | Raudel Avila[2,5,6] | Yoonseok Park[1,7]

[1]Department of Materials Science and Engineering, Kyung Hee University, Yongin, Republic of Korea | [2]Department of Mechanical Engineering, Rice University, Houston, Texas, USA | [3]Advanced Materials Division, Korea Research Institute of Chemical Technology, Daejeon, Republic of Korea | [4]Advanced Materials and Chemical Engineering, KRICT School, University of Science and Technology, Daejeon, Republic of Korea | [5]Rice Advanced Materials Institute, Rice University, Houston, Texas, USA | [6]Digital Health Institute, Rice University, Houston, Texas, USA | [7]Kyung Hee University, Seoul, Republic of Korea

Correspondence: Dong-Gyun Kim (dgkim@krict.re.kr) | Raudel Avila (ra88@rice.edu) | Yoonseok Park (yoonseok.park@khu.ac.kr)

Received: 24 March 2026 | **Revised:** 26 May 2026 | **Accepted:** 3 June 2026

Keywords: freestanding mesostructures | light-responsive soft robotics | material-independent integration | mechanically guided 3D assembly | physical anchoring

ABSTRACT

Mechanically guided 3D assembly has emerged as a powerful approach for constructing complex mesostructures, but conventional strategies rely on selective chemical bonding between 2D precursors and elastomeric substrates, restricting material compatibility and scalability. Here, we introduce a physical anchoring-based, buckling-guided assembly platform that decouples 3D structure formation from chemical adhesion. The platform employs an elastomeric substrate patterned with an array of rods to achieve robust mechanical fixation, enabling the integration of diverse functional materials, including polymers, metals, water-soluble polymers, and stimuli-responsive systems, independent of their interfacial or mechanical properties. Oxygen plasma surface treatment further reduces adhesion, allowing reliable assembly of freestanding and large-area architectures. As a proof-of-concept, we integrate liquid crystalline networks (LCNs) to demonstrate light-responsive soft robotic systems capable of remote actuation. This physically anchored assembly strategy establishes a general and scalable framework for mesoscale fabrication, expanding material and geometric design freedom for applications in soft robotics, bioelectronics, and multi-material integration.

1 | Introduction

Mechanically guided 3D assembly, which exploits controlled mechanical deformations such as folding [1–3], curving [4, 5], and buckling [6–9] to transform planar 2D precursors into complex 3D mesostructures, has emerged as a powerful strategy for fabricating multifunctional 3D architectures with high precision. This approach underpins diverse application areas, including bioelectronics [10, 11], healthcare [12, 13], MEMS [9, 14, 15], energy harvesting [16, 17], and soft robotics [1, 18, 19], by enabling the integration of architecturally complex 3D mesostructures with functional materials. Recent advances in 3D buckling-guided assembly expand this design space by either tailoring the geometric features of 2D precursors [14, 20–22] or tuning the mechanical properties of elastomeric substrates, for example, through thickness gradients or incorporation of stimuli-responsive elements [23–25]. Together, these strategies support the fabrication of

Yeonhee Heo, Pei Liu and Jeongmin Yoo contributed equally to this work.

high-resolution 3D architectures that adapt dynamically to mechanical loading. Conventional mechanically guided assembly methods rely on selective chemical bonding between the 2D precursor and the elastomeric substrate to maintain fixation during deformation. Transitioning bonded 3D structures into freestanding forms requires additional bonding-removal steps [26, 27] and the use of materials with sufficient rigidity to preserve their geometry after release [28, 29]. In conventional bonding-based assembly strategies, the integration of chemically inert materials remains challenging, and plasma or adhesive treatments often raise concerns regarding degradation of the intrinsic material functionalities. These limitations become particularly pronounced for biodegradable materials and stimuli-responsive polymers, whose mechanical and chemical properties are highly susceptible to surface modification processes. As a result, 3D architectures based on these materials, despite their strong potential in adaptive, responsive, and programmable systems, remain challenging to realize using conventional bonding-based assembly approaches and typically involve complex fabrication processes. These limitations highlight the need for an alternative assembly strategy that does not strictly depend on chemical adhesion but instead offers robust fixation, broad material compatibility, and scalability. Addressing this unmet need is essential to expand the design and material space of mechanically guided assembly, enabling freestanding 3D mesostructures from diverse materials and geometries that remain inaccessible with conventional bonding-based approaches.

To overcome these constraints, we introduce a buckling-guided assembly platform that relies on physical anchoring rather than chemical adhesion. The new platform employs a rod-array-patterned elastomeric substrate (RPES), in which silicone rods serve as discrete anchoring sites for mechanical fixation of 2D precursors. This physical anchoring eliminates the dependence on chemical adhesion, enabling stable 3D structure formation across a broad range of materials, including chemically inert and mechanically fragile systems. Precursor designs that incorporate holes for rod insertion further simplify assembly while preserving material functionality. In addition, oxygen plasma treatment of the substrate provides a straightforward means to modulate interfacial roughness and adhesion. Whereas such surface treatments destabilize chemically bonded systems [30], the physical anchoring framework leverages them to facilitate precursor release and suppress unwanted adhesion, thereby enabling reliable assembly of large-area 3D mesostructures with improved scalability and structural integrity.

This physically anchored, buckling-guided assembly strategy establishes a versatile foundation for 3D mesoscale fabrication by leveraging mechanical fixation and controlled buckling instabilities to guide structural transformation. By removing the constraints of chemical bonding, it enables material-agnostic integration and opens opportunities for process concepts that directly exploit mechanical properties, such as compliance, anisotropy, and shape-memory, to realize functional 3D mesostructures for applications in soft robotics, bioelectronics, and multi-material system integration.

2 | Results

2.1 | Mechanism of Elastomeric Substrate for the 3D Assembly Without Chemical Bonding

Figure 1a presents a schematic illustration and optical image of the elastomeric substrate designed for 3D assembly without chemical bonding. The rod-array–patterned elastomeric substrate (RPES) is fabricated by mold casting, in which an elastomeric polymer (Ecoflex 00–30, Smooth-On, Inc.) is deposited into an acrylic mold (Figure S1). Elastomeric rods imprinted onto the RPES are arranged at regular intervals, and their spacing can be tuned by mechanical deformation along the horizontal and vertical directions. During 3D assembly, the final device geometry depends on the degree of substrate relaxation; thus, quantitative analysis of this relaxation is critical for guiding structural design. We define the relaxation rate (RR) as:

$$\text{Relaxation rate, RR } (\%) = \frac{d_{max} - d_{relaxed}}{d_{max}} \times 100 \qquad (1)$$

where d_{max} is the rod spacing at maximum strain, and $d_{relaxed}$ is the rod spacing after loading the 2D precursor and fully relaxing the substrate. The Ecoflex-based RPES, fabricated via mold casting, exhibits high mechanical reliability and reusability (RR = 50%) under repeated deformation (Figure S2).

Figure 1b illustrates the assembly process of a 2D precursor into a 3D structure using the RPES. (i) The 2D precursor is prepared with holes that match the maximum rod spacing (d_{max}) of the RPES. (ii) The precursor is physically anchored to the substrate by aligning the rods within the holes. (iii) During substrate relaxation, the holes anchored to the rods act as the mechanical fixation sites between the 2D precursor and the elastomeric substrate. The compressive stress generated by the relaxing silicone substrate induces buckling, transforming the 2D precursor into a 3D structure [6]. (iv) Once fixed, the assembled 3D structure can be released directly from the substrate without any chemical bonding. At the alignment stage of the 2D precursor, a PDMS (Dow Corning, USA) stamp-based transfer process is employed (Figure 1c). Owing to its higher Young's modulus compared with the Ecoflex-based RPES, the PDMS stamp enables uniform compression of the substrate rods and facilitates transfer of the 2D precursor onto the RPES. Upon removal of the PDMS stamp, the compressed rods spontaneously pop up due to elastic recovery, thereby mechanically anchoring the 2D precursor and inducing buckling-guided 3D assembly (Figure S3). Our approach is versatile and can be extended to structures on the mesoscale, reaching several hundred micrometers. To demonstrate meso-scale 3D geometries, a meso-RPES is exploited, featuring rods with a diameter of 50 μm and an inter-rod spacing of 500 μm. Figure 1d shows finite element analysis (FEA) results and scanning electron microscopy (SEM) images of the assembled 3D mesostructure formed on the meso-scale RPES. The 2D precursor is composed of a 2 μm-thick PI layer and a 200 nm copper layer (Detailed in the Experimental section).

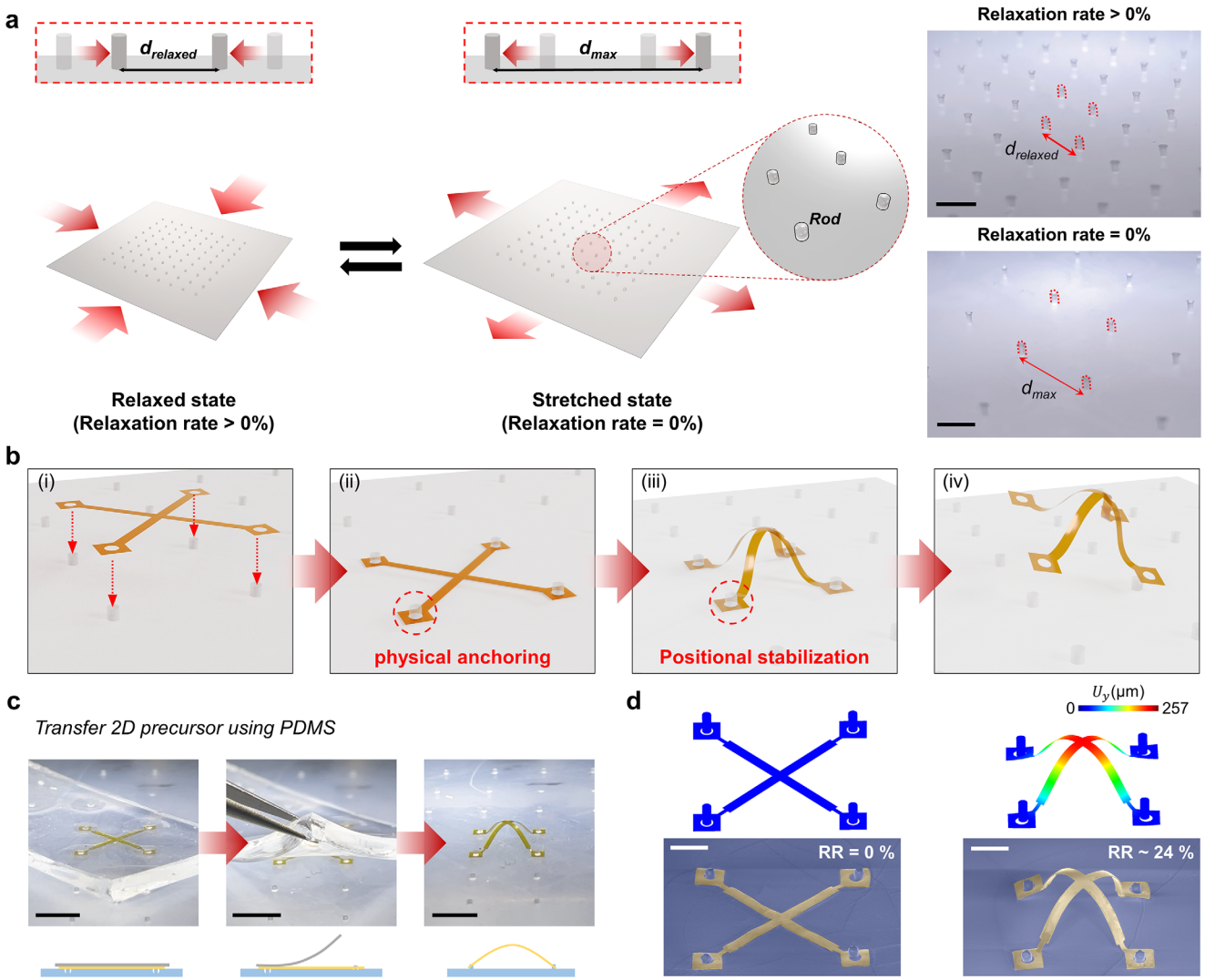

FIGURE 1 | Mechanism of buckling-guided assembly without chemical bonding. (a) Schematic and optical images of the rod-array-patterned elastic substrate (RPES). Scale bars, 5 mm. (b) Fabrication process diagram of freestanding 3D structures via buckling-guided assembly with physical anchoring: (i) Positioning the 2D precursor over the rods on the pre-stretched RPES.; (ii) fitting the 2D precursor's holes onto the rods on the RPES; (iii) relaxation of the stretched substrate; (iv) formation of a freestanding 3D structure through buckling-guided assembly without chemical bonding. (c) Optical images of PDMS stamp-assisted 2D precursor transfer onto the RPES, followed by buckling-guided 3D assembly. Scale bars, 5 mm. (d) FEA predictions and SEM images of 3D mesostructure. Scale bars, 200 μm.

2.2 | Design of Ribbon Structures With Various Ankle Geometries

The ribbon structure serves as a prototypical design, consisting of bonding sites at both ends (red regions), a central segment (green region), and connecting ankles between the segment and bonding sites. Variations in ankle geometry (width a, length L_a) determine the final transformed 3D configuration [22]. Modulating these design parameters enables precise control over the attachment and detachment mechanics behavior of bonding sites through physical anchoring, without reliance on conventional chemical bonding between the substrate and the 2D precursor. By adjusting the normalized ankle width ($2a/W$), both attached bonding site (AB) and detached bonding site (DB) configurations can be realized (Figure 2a).

Figure 2b presents the experimental results and finite element analysis (FEA) predictions of the relaxation rate required to induce detachment of bonding sites (RR_{DB}) as a function of ankle width. Here, RR_{DB} is defined as the point at which the angle between the bonding site and the substrate first exceeds 0°. The bonding site is classified as attached (AB, blue region) when below this threshold and detached (DB, orange region) when above it. The 2D precursor is fabricated from polyimide (PI) film (45 μm thickness), and the ankle length (L_a) is fixed at one-tenth of the middle segment length (L) ($2L_a/L = 0.2$). In the absence of an ankle ($2a/W = 0$), strain distributes across the entire structure, facilitating the transition from AB to DB and resulting in a low RR_{DB} value. As ankle width increases ($2a/W > 0$), strain localizes at the ankle, suppressing bonding site detachment and consequently leading to a higher RR_{DB} value (Figure S4).

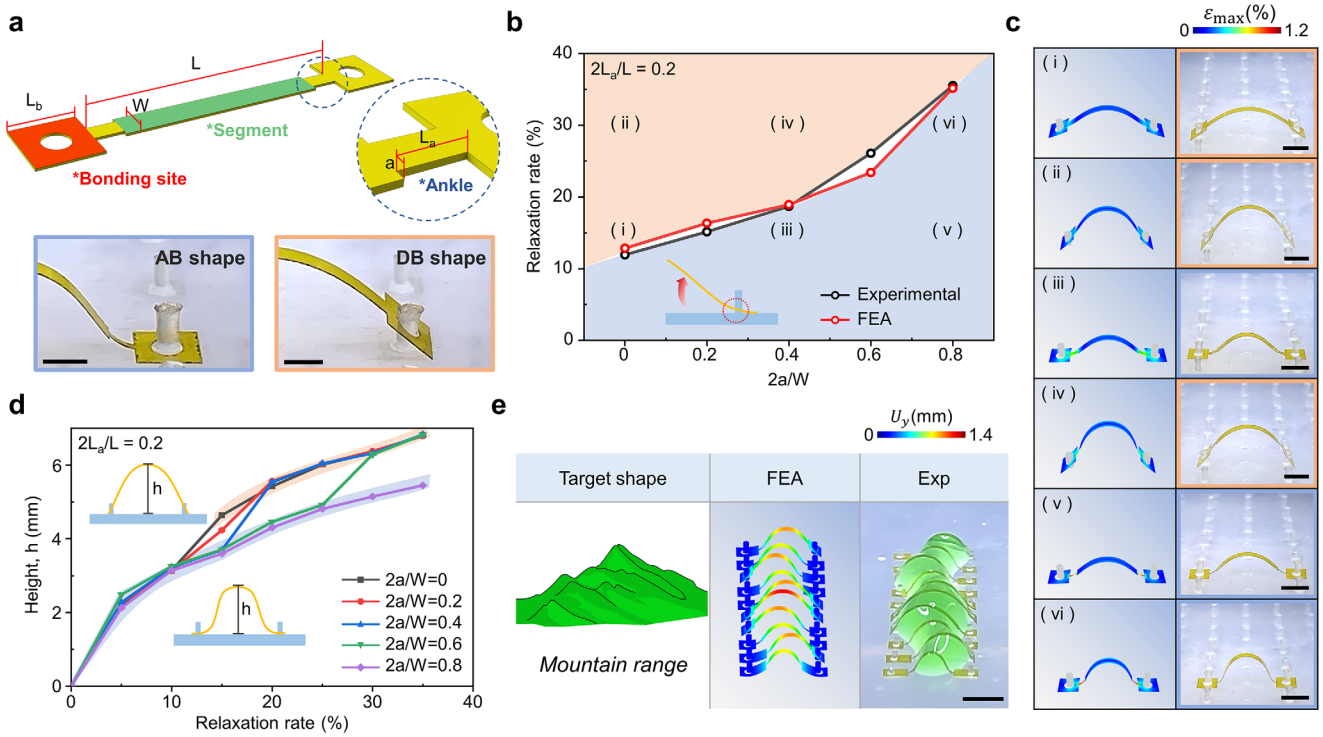

FIGURE 2 | Design of straight ribbon structures with ankle geometry. (a) Illustration of a straight ribbon with ankle (a, La) and Morphology of the straight ribbon depending on bonding site detachment (AB: attached bonding site, left; DB: detached bonding site, right). Scale bars, 2 mm. (b) Relationship between relaxation rate and bonding site detachment onset as a function of ankle ratio (2a/W), and corresponding FEA analysis (blue region: AB shape, orange region: DB shape). (c) Experimental images for Figure 2b (i–vi) and corresponding FEA predictions of strain distribution in the ankle. Scale bars, 4 mm. (d) Height of straight ribbon structures with various ankle ratios as a function of relaxation rate. (e) FEA analysis and Experimental image of a 3D mountain range shaped structure formed using various ribbon designs. Scale bars, 2 mm.

This trend appears consistently in both FEA predictions and experimental measurements. The strain concentration at the ankle is further visualized through FEA and optical images at representative relaxation rates RR (15% and 30%), confirming that the AB-DB transition is governed by the ankle design as shown in Figure 2c.

This mechanism enables two discrete height states controlled by the attachment or detachment of the bonding site. Experimental results confirm that adjusting only the ankle width produces distinct height configurations of 3D structures under identical RR conditions (Figure 2d). Furthermore, increasing the bonding site length (L_b) shortens the effective middle segment length, allowing finer mechanical control over the achievable height states (Figure S5).

Figure 2e shows FEA predictions and experimental images of a 3D mountain range structure assembled from ribbon arrays (Figure S6a). Each ribbon is independently defined by three geometric parameters: ankle width, asymmetric ankle placement, and bonding site length. Together, these parameters control the height and peak position of the ribbons (Figure S6b). FEA validation confirms the geometrical design rules, and diverse mountain range-like topographies with varying heights and peak locations are fabricated at a relaxation rate of 25% (Movie S1). These results demonstrate that a broad range of 3D morphologies can be achieved through geometric design of the 2D precursor, even with fixed rod positions and constant RR conditions.

2.3 | Mechanics Analysis of Post-Buckling-Induced Detachment

We develop a scaling analysis for post-buckling-induced detachment of a beam subjected to compressive relaxation strain (RR). The analysis isolates the effect of progressive loss of rotational constraint at the bonding sites, which governs the transition from the attached (AB) to detached (DB) configuration in Figure 2b. We model the middle segment as a slender multilayer Euler–Bernoulli beam of length L, width W, thickness t, and effective composite bending rigidity D_{eff}. The formulation applies to both homogeneous and multi-material precursors, including polyimide/copper (PI/Cu) bilayers commonly used in mechanically guided assembly. The beam undergoes axial compression from substrate relaxation in Equation (1). Deformation is assumed to occur in the weakly post-buckled regime, such that Euler–Bernoulli kinematics remain valid and geometric nonlinearity enters through the von Kármán axial strain. The governing equilibrium equation for transverse deflection $w(x)$ is

$$D_{\text{eff}} \frac{dw^4}{\mathrm{d}^4 x} + N \frac{dw^2}{\mathrm{d}^2 x} = 0 \tag{2}$$

$$D_{\text{eff}} = \sum_i E_i I_i + \sum_i E_i A_i (z_i - z_n)^2 \tag{3}$$

where D_{eff} is the effective flexural rigidity of the multilayer precursor, and N is the compressive axial force induced by the relaxation

strain. For multilayer precursors (e.g., copper/PI bilayers), the effective flexural rigidity follows classical laminated beam theory, where E_i, I_i, and A_i denote the Young modulus, second moment of area, and cross-sectional area of layer i, respectively, and z_n defines the neutral axis of the multilayer stack. The nonlinearity arises from the von Kármán kinematics associated with post-buckling deformation, while the multilayer flexural rigidity is treated within the framework of linear laminated beam theory.

In the attached (AB) state, the bonding site imposes a rotational constraint, which we approximate as clamped boundary conditions. As relaxation strain increases, bending moments concentrate near the anchoring region. Detachment does not represent a discontinuous change in geometric constraint, but rather a progressive reduction in effective rotational stiffness at the bonding interface. At small deformation, strong adhesion suppresses local rotation, and the interface behaves approximately as a clamped boundary. As post-buckling deformation increases, interfacial rotation becomes energetically favorable, leading to partial release of rotational constraint and an effective transition toward simply supported behavior. We treat this transition as a quasi-static stability problem. The critical relaxation rate corresponds to the point at which energetic relaxation of the rotational constraint becomes favorable relative to the constrained configuration. This condition defines the onset of post-buckling-induced detachment. In our previous work [31], we showed that a beam subjected to relaxation strain ε_{app} undergoes buckling when

$$\varepsilon_{app} > \varepsilon_c \tag{4}$$

where

$$\varepsilon_c = \frac{\pi^2 t^2}{3L^2} \tag{5}$$

is the classical Euler buckling strain for an in-plane compressed slender beam without substrate interaction. When strong adhesion is present, compression dominates, and buckling is suppressed. With increasing strain, the system may transition to localized buckling (wrinkling) before global buckling develops. In the present system, detachment occurs in the weak-adhesion regime, where global buckling governs the deformation. In the post-buckled state, the axial strain follows the von Kármán relation

$$\varepsilon \sim \frac{1}{2}\left(\frac{dw}{dx}\right)^2 \tag{6}$$

which for the fundamental mode of wavelength L yields the scaling

$$\varepsilon_{app} - \varepsilon_c \sim \frac{w^2}{L^2}. \tag{7}$$

The curvature scales as $\kappa \sim \frac{w}{L^2}$, giving a bending energy density per unit length as

$$u_{bend} = D_{\text{eff}}\,\kappa^2 \sim \frac{D_{\text{eff}}}{L^2}\left(\varepsilon_{app} - \varepsilon_c\right) \tag{8}$$

Integrating the energy density along the beam length yields the total bending energy

$$U_{bend} = \int_0^L u_{bend} dx \sim \frac{D_{\text{eff}}}{L}\left(\varepsilon_{app} - \varepsilon_c\right) \tag{9}$$

This scaling relation links the applied relaxation strain to the elastic energy stored in the post-buckled beam. At the scaling level, bending strain energy dominates the post-buckled response. Contributions from stretching and higher-order curvature localization remain small in the weakly nonlinear regime and are therefore neglected. At small applied strain, van der Waals interactions between the beam and the substrate impose a strong rotational constraint at the bonding sites. This condition is modeled as a clamped boundary at $x = 0$ and $x = L$.

$$\begin{cases} w = 0 \\ \frac{dw}{dx} = 0 \end{cases} \tag{10}$$

As the applied strain increases, the reaction moment at the bonding site grows and eventually exceeds the interfacial constraint, causing detachment. Following detachment, the boundary condition transitions to an effectively simply supported state

$$\begin{cases} w = 0 \\ \frac{d^2w}{dx^2} = 0 \end{cases} \tag{11}$$

To quantify the energetic consequence of the boundary-condition transition without explicitly resolving the interfacial mechanics, we introduce a dimensionless boundary factor χ defined as

$$U_{\text{clamped}} = \chi\, U_{\text{simp}} \tag{12}$$

where U_{simp} denotes the post-buckling bending energy of a beam with simply supported boundary conditions. For the first post-buckling mode, the clamped configuration stores substantially larger bending energy than the simply supported configuration because the rotational constraint imposes a shorter effective deformation wavelength. Specifically, the clamped mode $w_c \propto 1 - \cos(2\pi x/L)$ has half the wavelength of the simply supported mode $w_s \propto \sin(\pi x/L)$. At fixed end-shortening, this reduction in wavelength increases the characteristic curvature and yields approximately four times the bending energy, giving $\chi \approx 4$ for the idealized uniform-beam limit. Detachment occurs when the elastic energy released by relaxing the rotational constraint equals the adhesive energy required to separate the interface

$$U_{\text{clamped}} - U_{\text{simp}} = U_{\text{adh}} \tag{13}$$

where the adhesive energy associated with the detachment of the two bonding sites is $U_{\text{adh}} = 2\gamma_s A$ with γ_s defined as the interfacial adhesion energy density and A the contact area of each bonding site. Substituting the post-buckling bending energy scaling derived above in Equation (6) yields the detachment strain as

$$\varepsilon_{\text{detach}} - \varepsilon_c \sim \frac{\gamma_s A L}{(\chi - 1)\, D_{\text{eff}}} \tag{14}$$

To incorporate the effect of structural cuts that introduce partial rotational freedom at the anchoring site, we define the normalized geometric parameters

$$\alpha = \frac{2a}{W}\ ,\ \beta = \frac{2L_a}{L} \tag{15}$$

where a and L_a represent the cut width and cut length, respectively. The combined influence of cut geometry is captured through the dimensionless parameter

$$\eta = \alpha\sqrt{1-\beta} \tag{16}$$

which captures the range between the fully clamped limit (η0) and the simply supported limit (η1). Increasing η reduces the effective rotational stiffness at the boundary, thereby lowering the energetic penalty associated with rotation. At the scaling level, the ankle region can be interpreted as an effective rotational spring with stiffness k_θ, which continuously relaxes the rotational constraint at the bonding site. The corresponding rotational energy is $U_{\text{rot}} = \frac{1}{2}\ k_\theta\theta^2$ where $\theta \sim dw/dx$ denotes the local rotation at the anchoring site. To characterize the transition between fully constrained and released rotational states, we define the normalized rotational constraint parameter as

$$\lambda_\theta = \frac{k_\theta}{k_\theta + k_0}\ \sim\ (1-\eta)\,,k_0 \sim \frac{D_{\text{eff}}}{L} \tag{17}$$

$$\chi = 1 + 3\lambda_\theta\ \sim\ 1 + 3\,(1-\eta) \tag{18}$$

In the limit $k_\theta \gg k_0$, rotational deformation is strongly constrained, and the boundary approaches the clamped limit, giving $\chi \to 4$. Conversely, when $k_\theta \ll k_0$, the rotational stiffness becomes negligible, and the boundary approaches the simply supported limit, giving $\chi \to 1$. Substituting this relation into the detachment criterion yields the generalized scaling law for detachment

$$\varepsilon_{\text{detach}} - \varepsilon_c \approx \frac{\gamma_s AL}{3\,(1-\eta)\,D_{\text{eff}}} \tag{19}$$

For homogeneous beam precursors with $D_{\text{eff}} = EWt^3$, Equation (19) reduces to

$$\varepsilon_{\text{detach}} - \varepsilon_c \approx \left(\frac{\gamma_s}{Et}\right)\left(\frac{AL}{Wt^2}\right)\frac{1}{3\left(1-\frac{2a}{W}\sqrt{1-\frac{2L_a}{L}}\right)} \tag{20}$$

Although the absolute detachment strain depends on the specific material properties and multilayer architecture through the effective flexural rigidity D_{eff}, the energetic framework and scaling structure governing the transition between constrained and released states remain applicable across different multilayer systems.

To further clarify the locking mechanism that replaces chemical bonding, we consider the force balance between the elastic restoring force generated by the post-buckled precursor and the anchoring force provided by geometric confinement at the substrate rods. Here, F_{anchor} represents the confinement force associated with rod–hole contact and resistance to rotational release during post-buckling deformation. The effective restoring force scales with the energetic gradient associated with the post-buckled deformation

$$F_{\text{restoring}} = \frac{\partial U_{bend}}{\partial w} \approx \frac{D_{\text{eff}}}{L^3}w \tag{21}$$

Using the weakly nonlinear post-buckling relation $w/L = (\varepsilon_{\text{app}} - \varepsilon_c)^{1/2}$, the restoring force becomes

$$F_{\text{restoring}} \approx \frac{D_{\text{eff}}}{L^2}(\varepsilon_{\text{app}} - \varepsilon_c)^{1/2} \tag{22}$$

Stable mechanical locking requires the anchoring force supplied by the rod confinement to exceed the elastic restoring force of the buckled precursor $F_{\text{anchor}} > F_{\text{restoring}}$. Because the restoring force generates a bending moment at the anchoring site, stable locking equivalently requires the transmitted restoring moment to remain below the resisting moment associated with rod confinement. Increasing the ankle width $2a/W$or ankle length $2L_a/L$lowers the effective rotational stiffness, thereby reducing the restoring bending moment transmitted to the anchoring site during post-buckling deformation and mitigating instability-driven vertical snap-through.

To investigate geometric effects in the 3D structures, we combine numerical simulations with analytical modeling to predict detachment behavior and the corresponding failure domain. Failure governed by pillar geometry arises through two mechanisms: rotation-limited confinement and vertical pillar detachment. Figure S6a summarizes the key geometric parameters, including the pillar diameter D_{rod}, hole diameter D_{hole}, pillar height H_{pillar}, and structural lengths L_1 and L_2. These parameters determine the detachment angle θ, which evolves as the relaxation rate increases and governs the transition between stable anchoring and geometric detachment and failure. Rotation-limited confinement results from the rotation of the structure, which modifies its effective horizontal span as

$$D_x = D_{hole}\ \cos\theta \tag{23}$$

$$\cos\theta \le \frac{D_{\text{rod}}}{D_{\text{hole}}} \tag{24}$$

Figure S6b shows the maximum allowable rotation angle θ_{max} as a function of the diameter ratio $D_{\text{rod}}/D_{\text{hole}}$. As $D_{\text{rod}}/D_{\text{hole}} \to 1$, rotational freedom decreases and eventually vanishes. Vertical pillar detachment results when the rotation changes the vertical height of the structure

$$H = (L_1 + D_{\text{hole}})\ \sin\theta \tag{25}$$

$$(L_1 + D_{\text{hole}})\sin\theta \le H_{rod} \tag{26}$$

Stable locking additionally requires that the rotation angle remains below the geometric release threshold

$$\theta < \theta_{max} \tag{27}$$

$$\theta_{max} = \sin^{-1}\left(\frac{H_{rod}}{L_1 + D_{hole}}\right) \tag{28}$$

Figure S6c shows the minimum pillar height H_{rod} required to prevent detachment as a function of the structural length L_1. Finite element simulations in Figure S6d,e illustrate the sensitivity of the system to the dimensionless parameters D_{rod}/D_{hole} and D_{rod}/H_{rod}, which govern detachment behavior during buckling. When $D_{rod}/D_{hole} = 0.7$, the pillar rotates up to $\theta \approx 50°$ because geometric confinement is weak. As the diameters approach unity ($D_{rod}/D_{hole}1$), rotational freedom becomes progressively restricted, and the rotation angle rapidly approaches zero in Equation (28). Similarly, when $D_{rod}/H_{rod} \approx 1$, the pillar aspect ratio cannot accommodate the imposed rotational deformation. The resulting kinematic rotation induces vertical separation between the pillar and the structure, eliminating mechanical support and leading to an unstable configuration in which the structure snaps, as shown for the relaxation rate of 13.40%. Figure S7a shows that the detachment strain increases monotonically with the normalized ankle width $2a/W$. A comparison between the proposed scaling law, which captures the energetic competition associated with the boundary-condition transition from clamped to simply supported and Euler–Bernoulli beam predictions, shows strong agreement (Figure S7b) for representative values of $\beta = 0.2$, 0.4, and 0.6, spanning the relevant geometric design space.

2.4 | Physical Bonding-Driven 3D Assembly Without Material Constraints

The material versatility of the physical anchoring-based assembly method is evaluated by assembling 3D structures from diverse 2D precursor materials, including polymer film (Polyimide, PI, 12.5 μm thickness) (Movie S2), metal (Cu, 10 μm thickness), and water-soluble polymer (polyvinyl alcohol, PVA, 21 μm thickness). FEA predictions and corresponding optical images in Figure 3a demonstrate the robustness of the RPES platform for assembling these materials into stable 3D architectures. In contrast to thermally stable materials such as PI and Cu, PVA is generally incompatible with chemical bonding-based assembly due to its low thermal stability (below 300°C) [32, 33] and poor resistance to organic solvents used in photolithography processes. Physical anchoring circumvents these thermal and chemical limitations, enabling reliable 3D assembly of PVA. Moreover, PVA exhibits shape-memory behavior, arising from reversible hydrogen-bond formation and dissociation near its glass transition temperature ($T_g = 70°C$) [33]. Exploiting this property, we demonstrate fabrication of freestanding 3D PVA architectures with fixed geometries.

Under identical geometric designs, the 3D structures fabricated from different materials exhibit overall similar out-of-plane deformation behaviors, suggesting that the final assembled 3D configurations are primarily governed by geometric design and boundary conditions between the substrate and the 2D precursor. A representative quantitative comparison using copper structures provides support for the agreement between experimental measurements and FEA predictions. As shown in Figure 3b, the experimentally measured cross-sectional height profiles closely match the FEA predictions, confirming the structural predictability of the RPES platform (Figure S9).

These findings highlight the ability of the physical anchoring-based approach to expand material compatibility beyond conventional bonding strategies while preserving geometric predictability, thereby broadening the range of 2D precursors available for complex 3D mesostructure fabrication.

2.5 | Surface Treatment of Substrates for Structural Assembly With Large Area 2D Precursors

While physical anchoring-based assembly enables 3D structuring of diverse materials, scaling to large-area 2D precursors introduces interfacial challenges, as illustrated by the schematic and experimental image in Figure 4a. The interface between the elastomeric substrate and the 2D precursor is governed primarily by van der Waals interactions [34]. As the contact area increases, these interactions become dominant, raising the energy barrier for buckling initiation and leading to assembly failure.

To mitigate these effects and expand the design space, oxygen plasma treatment (200 W, 20 min) is applied to increase substrate surface roughness, thereby reducing interfacial van der Waals interactions. Figure 4b presents a schematic of the treatment process and optical microscopy images of the substrate surface after plasma exposure. Oxygen plasma introduces hydrophilic functional groups and generates micro-patterns on the surface through physical etching by oxygen ions [35]. Scanning electron microscopy (SEM) images confirm that the untreated silicone elastomer substrates exhibit smooth, featureless surfaces, whereas treated substrates display microgrooves with dimensions of ~4 μm (Figure 4c). Figure 4d shows peel strength measurements before and after surface treatment, performed by attaching a PI film (40 mm × 40 mm, 12.5 μm thickness) to the substrate and conducting a 90° peel test using a force measurement system (F105, Mark-10; Figure S10). Under various plasma treatment conditions, the peel strength is reduced by approximately 27% compared to untreated substrates (Figure S11). Both theoretical analysis and experimental demonstrations confirm that surface-treated RPES supports reliable assembly of large-area 2D precursors into complex geometries, including boxes, pyramids, and butterfly structures (Figure 4e; Figure S12).

2.6 | Light-Responsive Applications of 3D Liquid Crystalline Networks (LCN) Structures

The RPES imposes virtually no restrictions on material selection for 3D assembly, enabling straightforward integration of stimuli-responsive materials [36] into externally actuated structures. To demonstrate this versatility, we employed a liquid crystalline network (LCN) film to construct a 3D structure capable of reversible, directional deformation under light stimulation [37–39].

The LCN film (15 μm thickness) was fabricated from a mixture of mesogenic monomer (RM105), mesogenic crosslinker (RM257), dynamic crosslinker (MBTA), and a blue dopant dye (DB14) as a composite filler (Figure 5a; Figures S13 and S14). Under the elevated temperatures, LCN films with splay mesogen alignment undergo a phase transition to the isotropic state because the planarily aligned LCN part contracts, while the homeotropically aligned LCN part stretches, thereby exhibiting bending actuation [39, 40]. As a dopant dye, DB14 efficiently absorbs light at a wavelength of 660 nm and generates localized heat,

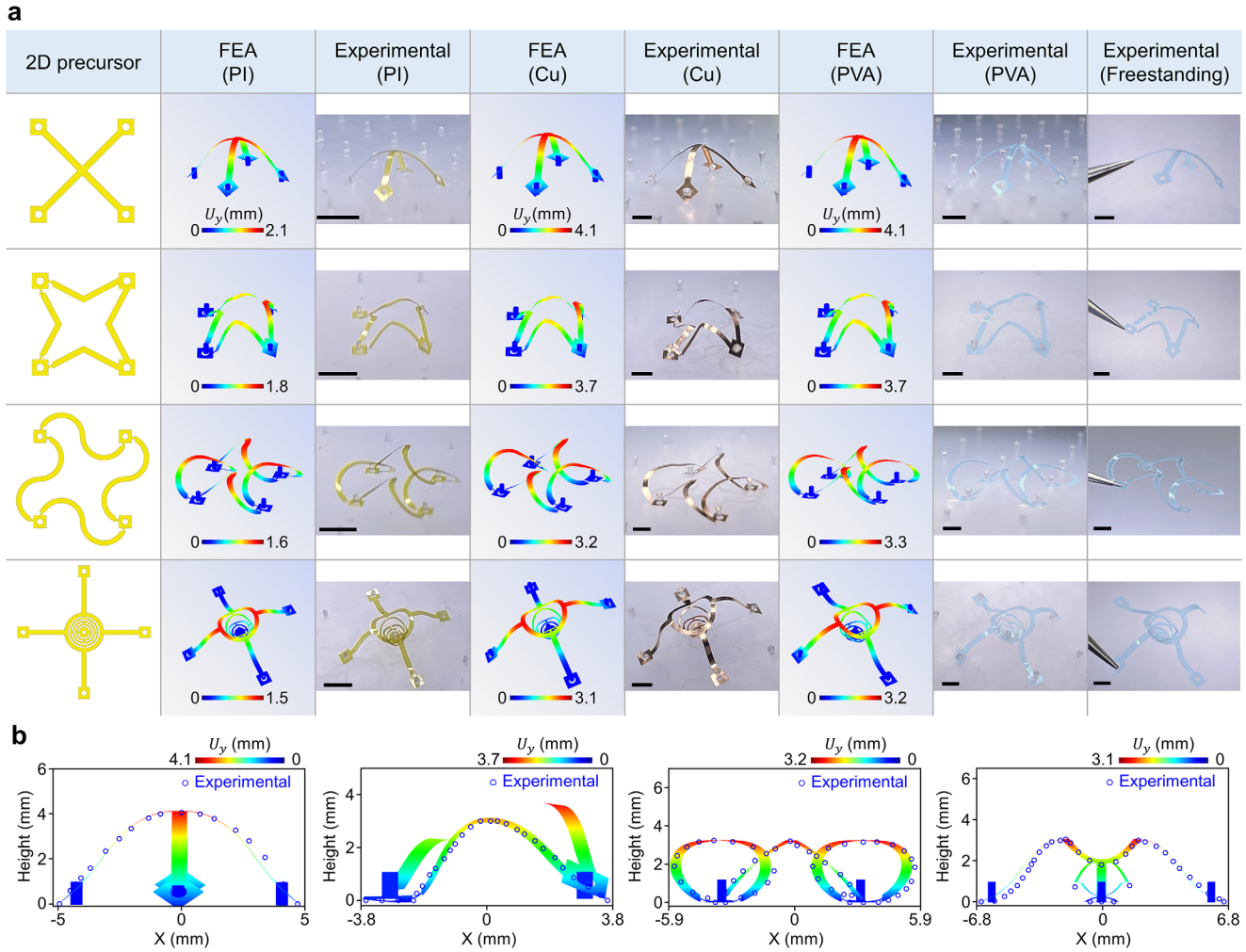

FIGURE 3 | Diverse 3D structures assembled from various materials on RPES. (a) FEA predictions and Experimental images of 3D structures fabricated using PI, Cu, and PVA thin films. Scale bars, 2 mm. (b) Quantitative height profile comparison between experimental and FEA results in 3D copper structures.

a phenomenon known as the photothermal effect (Figure S15) [40, 41]. Therefore, the 2D LCN film exhibits light-responsive bending actuation under 660 nm light irradiation (Figure 5b). In addition, due to the presence of the dynamic allyl sulfide bond exchangeable crosslinker MBTA, the LCN film demonstrates shape-reconfiguration capabilities through UV-induced rearrangement of the crosslinking junctions (Figure 5c) [41].

In contrast to previously reported chemical bonding-based assembly approaches, the physical anchoring-based assembly approach offers the capability to directly fabricate freestanding 3D structures from LCN films without requiring adhesive bonding or subsequent release steps, thereby simplifying the assembly workflow while preserving the intrinsic light-responsive actuation behavior of the material. The 2D precursor designs are engineered with mesogen alignment orientations that ensure targeted actuation performance. When assembled on the RPES platform and subsequently reconfigured, LCN-based 3D structures function as soft robotic systems, including a soft gripper, a soft crawling robot, and bioinspired shape-morphing structures (Figure 5d). Because rapid actuation and recovery are critical for soft robotics, we quantitatively analyzed the bending dynamics of the 3D LCN film. Under 660 nm light irradiation (MDL-III-660 laser, intensity ~0.2 W/cm^2), the films exhibit a response time of ~0.8 s and a recovery time of ~1.2 s, as measured by video-based angle tracking (Figure 5e; Figure S16a,b). These results highlight the rapid and reversible photothermal responses achievable through the integration of LCN films with the RPES platform.

Building on the actuating capabilities of 3D LCN films assembled via the RPES platform, we integrated these structures into soft robotic systems, including a soft gripper, a soft crawling robot, and bioinspired morphing architectures. As shown in Figure 5f, the soft gripper reliably grasps and lifts a lightweight polyurethane foam sample (0.01 g, Flex Foam, Smooth-On, Inc.) under 660 nm light irradiation. The practical force required for this task is 98 μN, falling well within the theoretical capacity (~180 mN) of the LCN structure, which ensures stable mechanical performance (Conversion efficiency: 0.0306%). For the soft crawling robot, asymmetrically configured leg lengths were introduced to enable light-driven locomotion. Upon exposure to 660 nm light, the longer leg undergoes a greater bending angle than the shorter leg, generating net forward displacement per actuation cycle. Repeated application and removal of the light stimulus

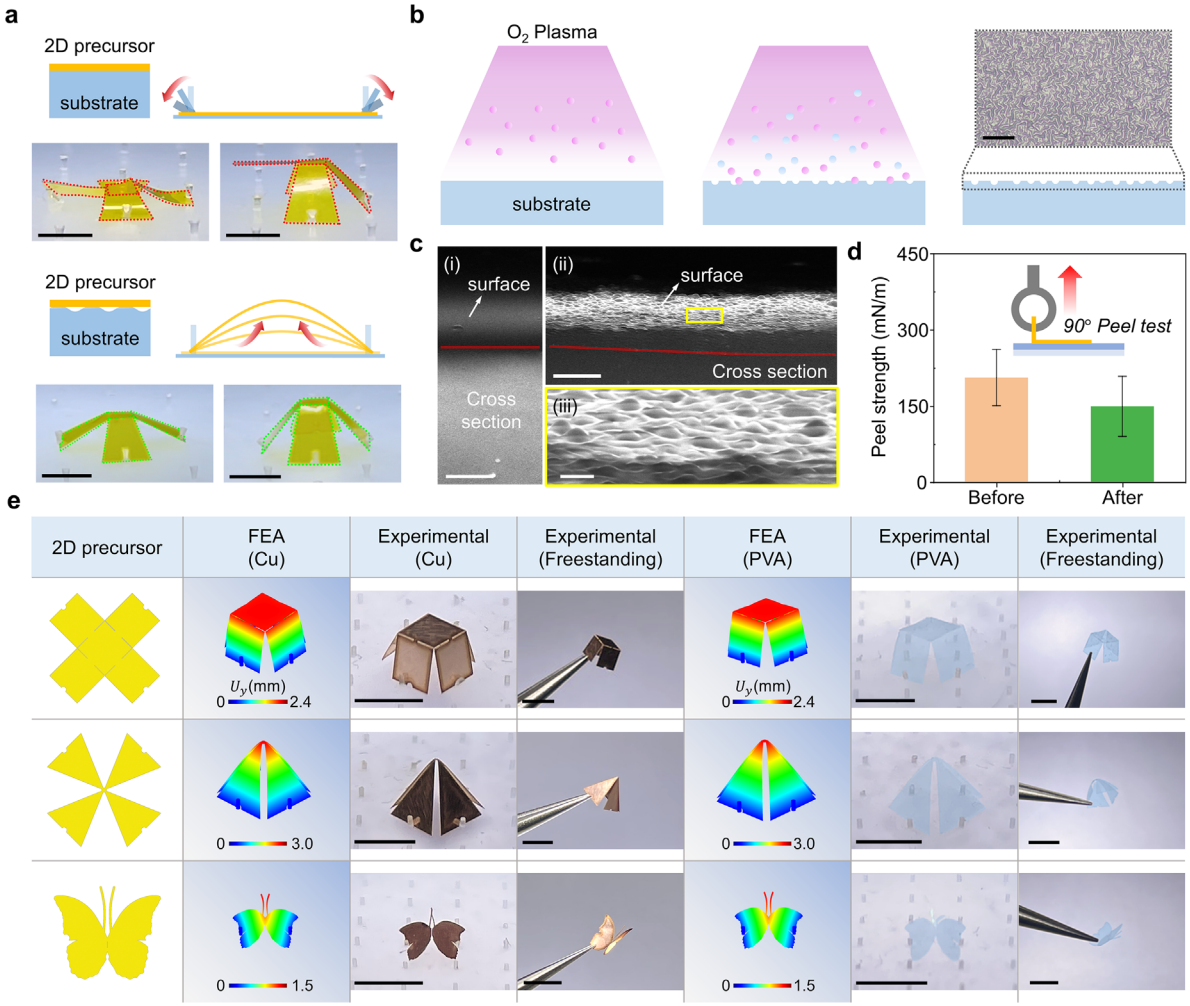

FIGURE 4 | Substrate surface treatment for assembly of large contact area 2D precursors into 3D structures. (a) Schematic illustration and experimental images comparing the assembly of large contact area structures on before and after surface-treated substrates. Scale bars, 2 mm (b) Process diagram of substrate surface treatment by O_2 plasma and Optical microscope images of substrate surface after treatment. Scale bar, 20 μm. (c) SEM images of substrate surfaces: (i) Untreated substrate, (ii) treated substrate, (iii) magnified view of the wrinkled microstructure in the treated substrate. Scale bars: 30 μm in (i, ii); 5 μm in (iii). (d) Quantitative comparison of interfacial peel strength before and after surface treatment evaluated using a 90° peel test. (e) FEA predictions and Experimental images of freestanding 3D structures; box shape; pyramid shape; butterfly shape. Scale bars, 4 mm.

result in a total displacement of ~7 mm (Figure 5g). Bio-inspired morphing structures, including flower and butterfly designs, are shown in Figure 5h. The butterfly is formed from a single film through directional cutting, whereas the flower is created by welding individually cut segments with distinct alignment orientations, enabling multi-directional petal actuation. Both structures replicate natural motions such as petal opening and wing flapping in response to 660 nm light irradiation (Movie S3).

This demonstration serves as a proof-of-concept that previously unexplored light-responsive polymers can be harnessed to achieve effective 3D structural assembly while preserving their intrinsic functional properties. These findings establish the physical anchoring-based assembly approach as a general and scalable platform for integrating diverse material classes into freestanding 3D architectures without loss of actuation performance.

3 | Conclusion

This study introduces a physically anchored assembly method and an elastomeric substrate platform as an alternative to conventional chemically bonded approaches for 3D structure fabrication. Experimental and theoretical validation confirm that this strategy enables the stable formation of 3D architectures without chemical bonding. The approach offers broad material compatibility, accommodating polymers, metals, and water-soluble polymers, thereby expanding material selection for mechanistic assembly beyond chemical or thermal constraints. Oxygen plasma surface treatment further reduces interfacial energy with large-area 2D precursors, enhancing reliability and scalability for complex geometries. In addition, integration of light-responsive liquid crystalline networks (LCN) demonstrates the platform's ability to fabricate and actuate functional 3D structures. Building upon the demonstrated capability, the developed physically anchored assembly strategy can be extended to diverse applications,

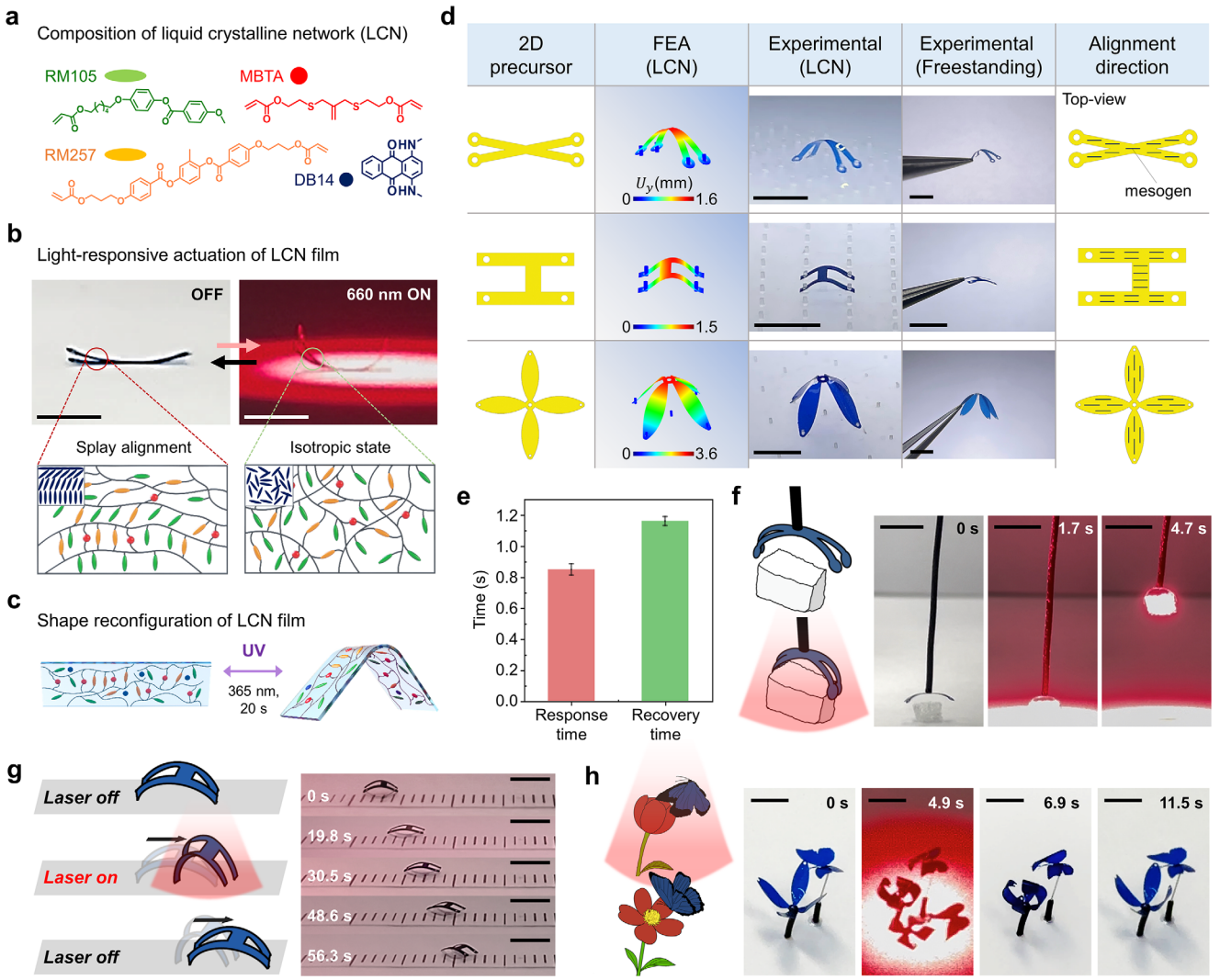

FIGURE 5 | Applications of light-responsive LCN film–based 3D structures. (a) Composition of liquid crystalline network (LCN). (b) Light-responsive bending actuation of the LCN film under 660 nm laser irradiation. Scale bars, 3 mm. (c) Schematic illustrations of LCN film showing shape reconfiguration under UV irradiation. (d) FEA predictions, experimental images, and bending direction of 3D structures. Scale bars, 4 mm. (e) Response and recovery times of the LCN film under the 660 nm laser irradiation. Schematic illustrations and optical images of soft LCN-based 3D structures including (f) a soft gripper, (g) a soft robot showing periodic bending motion, and (h) bioinspired forms mimicking flower blooming and butterfly wing flapping. Scale bars, 4 mm (f–h).

including 3D soft robotic actuators, stretchable electronic interfaces, and biodegradable bioelectronic platforms. The compatibility with previously inaccessible materials enables new routes for building multifunctional devices that combine structural complexity with tailored functionality. Overall, this work establishes a versatile and scalable 3D assembly strategy that not only broadens the accessible material selectivity for meso-scale fabrication but also provides a practical pathway toward next-generation adaptive 3D systems and bioelectronic device technologies.

4 | Experimental Section

4.1 | Mechanical Modeling of 3D Mesostructure Assembly

Finite element simulations were conducted using the commercial software ABAQUS 2023 to model the deterministic assembly and mechanical response of the system and quantify local strain distributions within 3D assembled mesostructures. A 3D quasi-static model was employed for all cases. Prior to releasing the pre-stretch of the soft substrate, a small displacement (~1% thickness) was applied to the precursor to induce an initial but small perturbation and trigger buckling upon mechanical relaxation. Frictionless contact is used to model the interfacial interaction between the substrate and the precursor. To account for interfacial bonding with the substrate, a separate contact criterion is adopted with a constant coefficient of friction $\mu = 0.7$ is defined between the precursor and the rod-array patterns. This value of the coefficient of friction is calibrated from the experimentally measured detachment point of the straight ribbon structure during assembly. Precursors were meshed using four-node reduced-integration shell elements (S4R). Both rod-array patterns and substrate were modelled as rigid bodies, with four-node shell elements (R3D4) and eight-node reduced-integration solid elements (C3D8R). The total number of elements in the

mechanical simulation is ~60,100 to ensure computational accuracy and convergence. Linear elastic material models, as well as idealized plastic models, are used to model the material properties of precursors, which are $E_{\mathrm{PI}} = 2.5$ GPa, $\nu_{\mathrm{PI}} = 0.34$, $\sigma_{PI} = 7.5$ MPa, and $t_{PI} = 12.5$ μm for polyimide (PI); $E_{\mathrm{Cu}} = 129$ GPa, $\nu_{\mathrm{Cu}} = 0.34$, $\sigma_{Cu} = 380$ MPa and $t_{Cu} = 10$ μm for copper (Cu), $E_{\mathrm{PVA}} = 12$ GPa, $\nu_{\mathrm{PVA}} = 0.45$, $\sigma_{PVA} = 35$ MPa, and $t_{PVA} = 15$ μm for Polyvinyl alcohol (PVA), and $E_{\mathrm{LCN}} = 2.41$ GPa, $\nu_{\mathrm{LCN}} = 0.45$, $\sigma_{LCN} = 30$ MPa, and $t_{LCN} = 30$ μm for liquid crystalline networks (LCN).

4.2 | Fabrication of 3D Structures Using RPES

The Rod-array-patterned elastomeric substrate (RPES) was fabricated via mold casting using a silicone elastomer (Ecoflex 00–30, Smooth-On, Inc.). Ecoflex 00–30 was used as received. Acrylic molds containing circular through-holes with defined spacing were fabricated by laser cutting. The thickness of the acrylic sheet determined the height of the resulting pillars. The acrylic mold was fixed to the base of a Petri dish to prevent leakage during casting. Ecoflex Part A and Part B were mixed at a 1:1 weight ratio and stirred thoroughly for 2 min. The mixture was poured into the molds, and air bubbles were removed by vacuum degassing for 5 min. The filled molds were cured at room temperature (~25°C) for 3 h. After curing, the elastomeric substrates were gently peeled from the molds.

The rod-array-patterned elastomeric substrate (RPES) was mounted onto a custom-built biaxial stretcher, which enabled uniform expansion of the rod array along both the horizontal and vertical axes. To assemble the 3D structure, the RPES was first subjected to stretching, reaching a predetermined strain that corresponded to a relaxation rate (RR) of 50%, thereby increasing the inter-rod spacing. The 2D precursor was precisely designed with anchoring hole positions matching the rod spacing at this maximum stretched state, ensuring accurate and stable engagement. The 2D precursors were patterned using a UV laser marker (ML-UVT LASER; 3 W, 355 nm, MACHINE SHOP). 2D precursors were prepared using commercial polyimide (PI, 12.5 μm thickness, COVALUEBIZ in the Republic of Korea), copper (Cu, 10 μm thickness), and fabricated PVA and LCN films (detailed in the Experimental section), with commercial materials used as received. Polydimethylsiloxane (PDMS, Dow Corning, USA) stamps for 2D precursor transfer were fabricated by mixing base (5 g) and curing agent (0.5 g), followed by curing at 60°C for 3 h in an oven. Following 2D precursor transfer and physical anchoring, the 2D precursor underwent compressive strain as the RPES was relaxed, inducing buckling deformation of the precursor and assembling it into a stable 3D structure. Surface treatment of the RPES was performed using a plasma processing system (CIONE4-LF-1MP; 13.56 MHz, FEMTO SCIENCE).

4.3 | Fabrication of Meso-Scale RPES

Silicon wafers were first coated with SU-8 100 (Kayaku Advanced Materials, Japan) by spin coating at 4000 rpm for 50 s, followed by soft baking at 65°C for 30 min and 95°C for 90 min. The films were then exposed for 55 s (9.1 mW), post-exposure baked at 65°C for 5 min and 95°C for 20 min, and developed for 20 min in SU-8 developer. After cleaning, the wafers were hard-baked at 150°C for 20 min to obtain the SU-8 molds. Meso-scale RPES were fabricated by casting a silicone elastomer (Ecoflex 00–30, Smooth-On, Inc.) onto the prepared SU-8 molds, followed by curing and demolding.

4.4 | Preparation of Meso-Scale 2D Precursor

The preparation of meso-scale 2D precursors began with spin coating a thin layer of poly(methyl methacrylate) (PMMA A8, Kayaku Advanced Materials, Japan) onto a clean glass slide at 3000 rpm for 30 s, followed by curing at 180°C for 30 s. A polyimide (PI) layer (Liquid PI, Sigma-Aldrich, USA) was then deposited by spin coating at 1000 rpm for 40 s and cured at 250°C for 1 h. The 2D precursors were patterned through photolithography processes. After a copper (Cu) hard mask (thickness: 200 nm) was deposited using a thermal evaporation system (DAEKI HI-TECH Co., Ltd.), the photoresist was stripped, and the exposed PI regions were etched by oxygen plasma etching (200 W, 15 min). Immersion in acetone overnight dissolved the underlying PMMA layer, thereby releasing the 2D precursors from the glass slide for subsequent transfer onto a PDMS stamp.

4.5 | Synthesis of PVA Film

Poly (vinyl alcohol) (PVA) powder (M_w 146,000-186,000, 99+% hydrolyzed, Sigma-Aldrich, USA) was used as received. First, PVA powder (0.15 g, ~3.4 mmol vinyl alcohol repeat units) was introduced into 20 g of deionized (DI) water. The mixture was heated in an oven at 90°C for 7 h to achieve complete dissolution of the PVA, thereby yielding a 0.75 w/v% PVA solution. Subsequently, the homogeneous solution was cast into a flat container and allowed to stand in an oven at 70°C overnight to complete the solution casting process and to form PVA films.

4.6 | Materials of LCN

4-Methoxybenzoic acid 4-(6-acryloyloxyhexyloxy)phenyl ester (RM105, 97%, Synthon Chemicals), 4-bis-[4-(3-acryloyloxypropyloxy)benzoyloxy]-2-methylbenzene (RM257, 97%, Synthon Chemicals), Disperse Blue 14 (DB14, dye content: 97%, Sigma-Aldrich), 2,2-dimethoxy-2-phenylacetophenone (Irgacure 651, DMPA, 99%, Sigma-Aldrich), 2-methylene-propane-1,3-bis(thioethyl acrylate) (MBTA, 99%, Uniotech), planar alignment layer-coated glass (40 × 30 × 0.7 mm, IDP System), homeotropic alignment layer-coated glass (30 × 30 × 0.7 mm, LC Tech), NOA63 UV-curing epoxy material (Norland Products), and 15 μm spacers (15 μm polymer microspheres, Suzhou Nanomicro Technology Co. Ltd.) were used as received. All other reagents and solvents were used as received from standard vendors.

4.7 | Preparation of LCN Film

For LC cell fabrication, a planar alignment layer on a glass substrate (4 cm × 3 cm) was used as the lower surface, while

a homeotropic alignment layer on a glass substrate (3 cm × 3 cm) was used as the upper surface. The homeotropic alignment layer-coated glass was placed above the planar layer-coated glass with polymer bead spacers, and NOA63 was added at the four corners and then cured using a 20 mW cm^{-2} UV LED ($\lambda = 365$ nm) to prepare a 15 μm-thick liquid crystal cell. For preparing LCN film, RM105 (0.4 g, 63 mol%), RM257 (0.22 g, 23.8 mol%), MBTA (0.05 g, 10.2 mol%), DB14 (0.004 g, 1 mol%), and Irgacure 651 (0.01 g, 2 mol%) were placed in a vial equipped with a magnetic stirring bar, followed by stirring at 100°C for 10 min to obtain a homogeneous reactive LC mixture. The prepared LC cell was placed on a hot plate at 80°C, and the LC mixture was infiltrated into the LC cell through capillary force. After infiltration, the LC cell was naturally cooled to 25°C at a rate slower than 5°C min^{-1}. Then, UV-induced photopolymerization was performed at 25°C (365 nm, 20 mW cm^{-2}) for 15 min. The crosslinked LCN film inside the LC cell was carefully separated using a blade.

4.8 | Instrumentation and Characterization Techniques of LCN Film

UV-Vis-NIR spectra were recorded on a Perkin-Elmer Lambda 365+ spectrometer. The temperature changes of LCNs during the visible light irradiation were monitored using an infrared camera (E54, FLIR). The single-wavelength laser source (MDL-III-660 laser, 660 nm, maximum intensity = 0.5 W cm^{-2}, CNI Optoelectronics Technology Co., Ltd.) was applied for visible light actuation. A UV LED (365 nm, maximum intensity = 8 W cm^{-2}, FE400, Phoseon Technology) was used for photopolymerization. The UV LED light (365 nm, 5 W, RM104, RAYMAN, China) was employed to induce shape reconfiguration. Scanning electron microscopy (SEM) was conducted on Tescan Mira 3 LMU FEG (Accelerating voltage: 10 kV).

4.9 | HR-SEM Setup for Substrate Surface Observation

To prepare clean cross-sections, both oxygen plasma-treated and untreated samples were immersed in liquid nitrogen and subsequently fractured. To minimize sample charging and enhance secondary electron emission, the samples were then subjected to platinum (Pt) sputtering for 3 min. Observations were performed using a high-resolution scanning electron microscope (HR-SEM, MERLIN, Carl Zeiss) at an accelerating voltage of 10 kV and a working distance of 5 mm.

4.10 | Measurement of Peel Strength

The adhesive strength between the elastomeric substrate and the 2D precursor, before and after oxygen plasma treatment, was evaluated using 90° peel tests. Ecoflex 00–30 (Smooth-On, Inc.) parts A and B were mixed in a 1:1 weight ratio and spin-coated onto glass slides at 500 rpm for 45 s. One of the Ecoflex-coated substrates was then subjected to oxygen plasma treatment (200 W, 20 min). PI film samples (40 mm × 40 mm, 12.5 μm thickness) were prepared and attached to the treated and untreated substrates. The peel strength between the substrate and PI film was measured using a force measurement system (F105, Mark-10), with the peeling rate set to 13 mm/min in the upward direction.

4.11 | Video-Based Quantification of Bending Angle Using Python and OpenCV

Quantitative analysis of bending actuation dynamics was performed using a custom Python script based on the OpenCV library. For each video, three manually specified regions of interest (ROIs) were selected in the initial frame, corresponding to the two endpoints and the fixed center of the actuated structure. The coordinates of these reference points, defined as the centers of the ROIs, were automatically tracked throughout the video sequence using the CSRT object tracking algorithm implemented in OpenCV. For each frame, the coordinates of the left endpoint, right endpoint, and the fixed central point were determined. The instantaneous bending angle was then calculated using the geometric relationship between these three points, applying the law of cosines. Time-stamped angle data were recorded for each frame, using the known video frame rate to align angular measurements with real time. The resulting angle-time profiles enabled the quantitative assessment of response and recovery dynamics. This automated video-based quantification allowed for high-throughput, objective, and reproducible measurement of dynamic bending behavior in soft actuators.

Author Contributions

Y.H. and P.L. performed the designs and engineering investigation of the devices. Y.H., J.Y., J.H.W, G.C., D.-G.K. manufactured the 3D mesostructures. Y.H. was responsible for the original drafting of the manuscript. J.Y., R.A. and Y.P. assisted in critical editing and review of the final manuscript.

Acknowledgements

This work was supported by a grant from Kyung Hee University in 2022 (KHU-20220916).

Conflicts of Interest

The authors declare no conflicts of interest.

Data Availability Statement

The data that support the findings of this study are available in the supplementary material of this article.

References

1. Y. Sun, D. Li, M. Wu, et al., "Origami-Inspired Folding Assembly of Dielectric Elastomers for Programmable Soft Robots," *Microsystems & Nanoengineering* 8, no. 1 (2022): 37, https://doi.org/10.1038/s41378-022-00363-5.

2. G. Chung, J. W. Chae, D.-S. Han, S. M. Won, and Y. Park, "Reprogrammable, Recyclable Origami Robots Controlled by Magnetic Fields," *Advanced Intelligent Systems* 6, no. 10 (2024): 2400082, https://doi.org/10.1002/aisy.202400082.

3. Q. Liu, W. Wang, M. F. Reynolds, et al., "Micrometer-Sized Electrically Programmable Shape-Memory Actuators for Low-Power Microrobotics," *Science Robotics* 6, no. 52 (2021): abe6663, https://doi.org/10.1126/scirobotics.abe6663.

4. G. Zabow, "Reflow Transfer for Conformal Three-Dimensional Microprinting," *Science* 378, no. 6622 (2022): 894–898, https://doi.org/10.1126/science.add7023.

5. K. Sim, S. Chen, Z. Li, et al., "Three-Dimensional Curvy Electronics Created Using Conformal Additive Stamp Printing," *Nature Electronics* 2, no. 10 (2019): 471–479, https://doi.org/10.1038/s41928-019-0304-4.

6. S. Xu, Z. Yan, K.-I. Jang, et al., "Assembly of Micro/Nanomaterials into Complex, Three-Dimensional Architectures by Compressive Buckling," *Science* 347, no. 6218 (2015): 154–159, https://doi.org/10.1126/science.1260960.

7. X. Guo, X. Wang, D. Ou, et al., "Controlled Mechanical Assembly of Complex 3D Mesostructures and Strain Sensors by Tensile Buckling," *npj Flexible Electronics* 2, no. 1 (2018): 14, https://doi.org/10.1038/s41528-018-0028-y.

8. H. Luan, Q. Zhang, T.-L. Liu, et al., "Complex 3D Microfluidic Architectures Formed by Mechanically Guided Compressive Buckling," *Science Advances* 7, no. 43 (2021): abj3686, https://doi.org/10.1126/sciadv.abj3686.

9. H. Fu, K. Nan, W. Bai, et al., "Morphable 3D Mesostructures and Microelectronic Devices by Multistable Buckling Mechanics," *Nature Materials* 17, no. 3 (2018): 268–276, https://doi.org/10.1038/s41563-017-0011-3.

10. D. E. Fullenkamp, W.-Y. Maeng, S. Oh, et al., "Simultaneous Electromechanical Monitoring in Engineered Heart Tissues Using a Mesoscale Framework," *Science Advances* 10, no. 37 (2024): ado7089, https://doi.org/10.1126/sciadv.ado7089.

11. Y. Park, C. K. Franz, H. Ryu, et al., "Three-Dimensional, Multifunctional Neural Interfaces for Cortical Spheroids and Engineered Assembloids," *Science Advances* 7, no. 12 (2021): abf9153, https://doi.org/10.1126/sciadv.abf9153.

12. Y. Park, H. Luan, K. Kwon, et al., "Soft, Full Wheatstone Bridge 3D Pressure Sensors for Cardiovascular Monitoring," *npj Flexible Electronics* 8, no. 1 (2024): 6, https://doi.org/10.1038/s41528-024-00294-3.

13. S. M. Won, H. Wang, B. H. Kim, et al., "Multimodal Sensing with a Three-Dimensional Piezoresistive Structure," *ACS Nano* 13, no. 10 (2019): 10972–10979, https://doi.org/10.1021/acsnano.9b02030.

14. Z. Yan, F. Zhang, F. Liu, et al., "Mechanical Assembly of Complex, 3D Mesostructures from Releasable Multilayers of Advanced Materials," *Science Advances* 2, no. 9 (2016): 1601014, https://doi.org/10.1126/sciadv.1601014.

15. F. Liu, Y. Chen, H. Song, et al., "High Performance, Tunable Electrically Small Antennas Through Mechanically Guided 3D Assembly," *Small* 15, no. 1 (2019): 1804055, https://doi.org/10.1002/smll.201804055.

16. K. Nan, S. D. Kang, K. Li, et al., "Compliant and Stretchable Thermoelectric Coils for Energy Harvesting in Miniature Flexible Devices," *Science Advances* 4, no. 11 (2018): aau5849, https://doi.org/10.1126/sciadv.aau5849.

17. J. Yea, J. Ha, K. S. Lim, et al., "Curvature-Specific Coupling Electrode Design for a Stretchable Three-Dimensional Inorganic Piezoelectric Nanogenerator," *ACS Nano* 18, no. 50 (2024): 34096–34106, https://doi.org/10.1021/acsnano.4c09933.

18. M. Han, X. Guo, X. Chen, et al., "Submillimeter-Scale Multimaterial Terrestrial Robots," *Science Robotics* 7, no. 66 (2022): abn0602, https://doi.org/10.1126/scirobotics.abn0602.

19. W. Pang, S. Xu, J. Wu, et al., "A Soft Microrobot with Highly Deformable 3D Actuators for Climbing and Transitioning Complex Surfaces," *Proceedings of the National Academy of Sciences* 119, no. 49 (2022): 2215028119, https://doi.org/10.1073/pnas.2215028119.

20. X. Cheng, Z. Fan, S. Yao, et al., "Programming 3D Curved Mesosurfaces Using Microlattice Designs," *Science* 379, no. 6638 (2023): 1225–1232, https://doi.org/10.1126/science.adf3824.

21. Z. Fan, Y. Yang, F. Zhang, et al., "Inverse Design Strategies for 3D Surfaces Formed by Mechanically Guided Assembly," *Advanced Materials* 32, no. 14 (2020): 1908424, https://doi.org/10.1002/adma.201908424.

22. Y. Shi, F. Zhang, K. Nan, et al., "Corrigendum to "Plasticity-Induced Origami for Assembly of Three Dimensional Metallic Structures Guided by Compressive Buckling"[Extreme Mech. Lett. 11 (2017) 105–110]," *Extreme Mechanics Letters* 11 (2017): 105–110, https://doi.org/10.1016/j.eml.2016.11.008.

23. Y. Li, C. Luo, K. Yu, and X. Wang, "Remotely Controlled, Reversible, On-Demand Assembly and Reconfiguration of 3D Mesostructures via Liquid Crystal Elastomer Platforms," *ACS Applied Materials & Interfaces* 13, no. 7 (2021): 8929–8939, https://doi.org/10.1021/acsami.0c21371.

24. H. Luan, X. Cheng, A. Wang, et al., "Design and Fabrication of Heterogeneous, Deformable Substrates for the Mechanically Guided 3D Assembly," *ACS Applied Materials & Interfaces* 11, no. 3 (2019): 3482–3492, https://doi.org/10.1021/acsami.8b19187.

25. C. Zhang, H. Deng, Y. Xie, C. Zhang, J.-W. Su, and J. Lin, "Stimulus Responsive 3D Assembly for Spatially Resolved Bifunctional Sensors," *Small* 15, no. 51 (2019): 1904224, https://doi.org/10.1002/smll.201904224.

26. X. Wang, X. Guo, J. Ye, et al., "Freestanding 3D Mesostructures, Functional Devices, and Shape-Programmable Systems Based on Mechanically Induced Assembly with Shape Memory Polymers," *Advanced Materials* 31, no. 2 (2019): 1805615, https://doi.org/10.1002/adma.201805615.

27. Z. Yan, M. Han, Y. Shi, et al., "Three-Dimensional Mesostructures as High-Temperature Growth Templates, Electronic Cellular Scaffolds, and Self-Propelled Microrobots," *Proceedings of the National Academy of Sciences* 114, no. 45 (2017): E9455–E9464, https://doi.org/10.1073/pnas.1713805114.

28. Y. Park, H. Luan, K. Kwon, et al., "Transformable, Freestanding 3D Mesostructures Based on Transient Materials and Mechanical Interlocking," *Advanced Functional Materials* 29, no. 40 (2019): 1903181, https://doi.org/10.1002/adfm.201903181.

29. R. Bo, S. Xu, Y. Yang, and Y. Zhang, "Mechanically-Guided 3D Assembly for Architected Flexible Electronics," *Chemical Reviews* 123, no. 18 (2023): 11137–11189, https://doi.org/10.1021/acs.chemrev.3c00335.

30. K. Chau, B. Millare, A. Lin, et al., "Dependence of the Quality of Adhesion between Poly(dimethylsiloxane) and Glass Surfaces on the Composition of the Oxidizing Plasma," *Microfluidics and Nanofluidics* 10, no. 4 (2011): 907–917, https://doi.org/10.1007/s10404-010-0724-y.

31. A. Wang, R. Avila, and Y. Ma, "Mechanics Design for Buckling of Thin Ribbons on an Elastomeric Substrate Without Material Failure," *Journal of Applied Mechanics* 84, no. 9 (2017): 094501, https://doi.org/10.1115/1.4037149.

32. W. Wang, Y. Gong, Q. Sun, L. Li, A. Xu, and R. Liu, "High Performance Polyvinyl Alcohol/Polylactic Acid Materials: Facile Preparation and Improved Properties," *Journal of Applied Polymer Science* 139, no. 26 (2022): 52470, https://doi.org/10.1002/app.52470.

33. C. Tsioptsias, D. Fardis, X. Ntampou, I. Tsivintzelis, and C. Panayiotou, "Thermal Behavior of Poly(vinyl alcohol) in the Form of Physically Crosslinked Film," *Polymers* 15, no. 8 (2023): 1843.

34. Y. Liu, X. Wang, Y. Xu, et al., "Harnessing the Interface Mechanics of Hard Films and Soft Substrates for 3D Assembly by Controlled Buckling," *Proceedings of the National Academy of Sciences* 116, no. 31 (2019): 15368–15377, https://doi.org/10.1073/pnas.1907732116.

35. B. N. Sahoo, J. Woo, H. Algadi, J. Lee, and T. Lee, "Superhydrophobic, Transparent, and Stretchable 3D Hierarchical Wrinkled Film-Based Sensors for Wearable Applications," *Advanced Materials Technologies* 4, no. 10 (2019): 1900230, https://doi.org/10.1002/admt.201900230.

36. M. Wei, Y. Gao, X. Li, and M. J. Serpe, "Stimuli-Responsive Polymers and Their Applications," *Polymer Chemistry* 8, no. 1 (2017): 127–143, https://doi.org/10.1039/C6PY01585A.

37. C. L. van Oosten, C. W. M. Bastiaansen, and D. J. Broer, "Printed Artificial Cilia from Liquid-Crystal Network Actuators Modularly Driven

by Light," *Nature Materials* 8, no. 8 (2009): 677–682, https://doi.org/10.1038/nmat2487.

38. S. Iamsaard, S. J. Aßhoff, B. Matt, et al., "Conversion of Light into Macroscopic Helical Motion," *Nature Chemistry* 6, no. 3 (2014): 229–235, https://doi.org/10.1038/nchem.1859.

39. O. M. Wani, H. Zeng, and A. Priimagi, "A light-Driven Artificial Flytrap," *Nature Communications* 8, no. 1 (2017): 15546, https://doi.org/10.1038/ncomms15546.

40. M. Lahikainen, H. Zeng, and A. Priimagi, "Reconfigurable Photoactuator through Synergistic Use of Photochemical and Photothermal Effects," *Nature Communications* 9, no. 1 (2018): 4148, https://doi.org/10.1038/s41467-018-06647-7.

41. J. H. Hwang, J. Shin, J. Han, et al., "Monolithically Assembled 3D Soft Transformable Robot," *Advanced Intelligent Systems* 4, no. 9 (2022): 2200051, https://doi.org/10.1002/aisy.202200051.

Supporting Information

Additional supporting information can be found online in the Supporting Information section.

Supporting File 1: smll74211-sup-0001-SuppMat.docx.

Supporting File 2: smll74211-sup-0002-MovieS1.mp4.

Supporting File 3: smll74211-sup-0003-MovieS2.mp4.

Supporting File 4: smll74211-sup-0004-MovieS3.mp4.